

Temperature Structure and Mass-Temperature Scatter In Galaxy Clusters

David A. Ventimiglia¹, G. Mark Voit¹, E. Rasia^{2,3}

ABSTRACT

Precision cosmology studies based on wide-field surveys of galaxy clusters benefit from constraints on intrinsic scatter in mass-observable relationships. In principle, two-parameter models combining direct measurements of galaxy cluster structural variation with mass proxies such as X-ray luminosity and temperature can be used to constrain scatter in the relationship between the mass proxy and the cluster's halo mass and to measure the redshift evolution of that scatter. One candidate for quantifying cluster substructure is the ICM temperature inhomogeneity inferred from X-ray spectral properties, an example of which is T_{HBR} , the ratio of hardband to broadband spectral-fit temperatures. In this paper we test the effectiveness of T_{HBR} as an indicator of scatter in the mass-temperature relation using 118 galaxy clusters simulated with radiative cooling and feedback. We find that, while T_{HBR} is correlated with clusters' departures $\delta \ln T_X$ from the mean M - T_X relation, the effect is modest.

Subject headings: galaxies: clusters: general, X-rays: galaxies: clusters

1. Introduction

Galaxy clusters play an important role in precision cosmology that complements other techniques like Type Ia supernovae luminosity-distance relation measurements (Perlmutter et al. 1999; Riess et al. 1998), baryonic acoustic oscillations (BAOs) angular-distance relation measurements (Eisenstein et al. 2005), and observations of the cosmic microwave background radiation (see Frieman et al. (2008) for a review). For example, Vikhlinin et al. (2009) exploit

¹Michigan State University, Physics & Astronomy Dept., East Lansing, MI 48824-2320; ventimig@msu.edu, voit@pa.msu.edu

²Dept. of Astronomy, University of Michigan, Ann Arbor, MI 48109, USA

³Chandra Fellow

dark energy’s influence on the growth of structure by using 37 moderate-redshift and 49 low-redshift clusters to measure the shape of the galaxy-cluster mass function and its redshift evolution, which constrain the dark-energy density parameter Ω_Λ to 0.83 ± 0.15 in a non-flat Λ CDM cosmology and the dark energy equation of state parameter w_0 to -1.14 ± 0.21 in a flat cosmology. Mantz et al. (2010) have obtained similar results from measurements of the evolving number density of the largest clusters in order to constrain w_0 to -1.01 ± 0.20 .

Strategies like these that compare model predictions to galaxy-cluster sample statistics inevitably confront sample error and sample bias. Future surveys expected to gather samples of 10–40 thousand galaxy clusters¹ will maximize survey reach while maintaining sufficient observation quality in order to minimize sample error, but they still must grapple with a major source of sample bias, which is scatter in the relationship used to infer cluster mass from an observable mass proxy. An important mass-observable relation for galaxy cluster studies connects dark matter halo mass to the temperature of the intracluster medium (ICM) inferred from its X-ray spectrum (its “X-ray temperature” T_X). In this paper we investigate the possibility of correcting for scatter in this relation using temperature-inhomogeneity in the ICM, and discuss challenges that may exist in such a program.

A significant amount of uncertainty in the dark-energy constraints obtainable from large cluster surveys derives from uncertainty in scatter about the mean scaling relations obeyed by galaxy clusters’ bulk properties (Lima & Hu 2005; Cunha & Evrard 2010). The key galaxy cluster property to measure when trying to constrain dark energy with clusters is the cluster’s mass, which cannot be directly observed. Theoretical considerations predict correlations among halo mass and more readily observed cluster properties, like its galaxy richness, the velocity dispersion of its galaxies, T_X , the Sunyaev-Zel’dovich decrement, the gas mass, and Y_X parameter, which is the product of T_X and the gas mass inferred from X-ray observations (Kravtsov et al. 2006). Theory also predicts intrinsic scatter in these relations owing to variation in cluster dynamical state (see, for example Stanek et al. 2011; Fabjan et al. 2011; Rasia et al. 2011).

One way to deal with intrinsic scatter is to join a cluster model to a cosmological model and simultaneously fit for the parameters of both, leveraging the statistical power of large surveys and “self-calibrating” the mass-observable relations. Another approach is to combine observables that tend to depart from the expected scaling relations in opposite ways, yielding a new, low-scatter composite observable. An example low-scatter composite observable is Y_X , since at a given halo mass, offsets in the measured gas mass at fixed total mass tend to anti-correlate with offsets in the measured temperature (Kravtsov et al. 2006).

¹<http://www.mpe.mpg.de/heg/www/Projects/EROSITA/main.html>

Another family of low-scatter composite observables attempt to measure structural variation directly. Mergers, relaxation, and non-adiabatic processes like radiative cooling, star formation, and feedback ought to leave a visible imprint that may allow us to measure and correct for scatter. For example, one might use imaging to quantify resolved morphological substructure. Jeltema et al. (2008) apply two observationally-motivated structure measures, the power ratios (Buote & Tsai 1995) and the centroid shift (Mohr et al. 1993), to a sample of galaxy clusters simulated with *Enzo* (Norman & Bryan 1999; O’Shea et al. 2004). They find that cluster structure correlates strongly with bias in mass estimates derived from T_X under the assumption of hydrostatic equilibrium and accounting for cluster structure can be used to correct some of the bias. Similarly, Ventimiglia et al. (2008) apply the power ratios, centroid shift, and axial ratio (O’Hara et al. 2006) substructure measures to the same sample of simulated clusters used in this paper, and find that cluster substructure correlates with departures from the mean M - T_X relationship in the sense that clusters with more substructure tend to have a lower temperature at a given mass, and can be used to refine mass estimates derived from the ICM X-ray temperature. Piffaretti & Valdarnini (2008) likewise find that greater substructure, as quantified with power ratios, correlates with lower temperature at a given mass. Yang et al. (2009) find a strong correlation between mass-temperature scatter and halo concentration in their sample of simulated clusters, with cooler clusters appearing more concentrated than warmer clusters at similar mass.

Jeltema et al. (2008) observe, however, that line-of-sight projection effects lead to significant uncertainties in morphologically-derived substructure measures. Substructure also becomes more difficult to resolve at high redshift. Spectral signatures of dynamical state are therefore attractive because they are aspect-independent and redshift-independent. One such spectral signature of dynamical state is the “temperature ratio” T_{HBR} (Mathiesen & Evrard 2001; Cavagnolo et al. 2008), which divides a “hardband” spectral-fit temperature by a “broadband” spectral-fit temperature. An energy cut applied to a broadband spectrum produces a hardband spectrum and serves to filter out cooler line-emitting components of the ICM. Mathiesen & Evrard (2001) studied the effects of relaxation on the observable properties of galaxy clusters, using a sample of numerically-simulated galaxy clusters generated by Mohr & Evrard (1997). They found that hardband (2.0–9.0 keV) X-ray spectral fit temperatures average $\sim 20\%$ higher than broadband (0.5–9.0 keV) temperatures and suggested that this effect may signal the presence of cool, luminous sub-clusters lowering the broadband temperature. Valdarnini (2006) corroborated these findings in simulations that included radiative cooling.

Figures 1 and 2 illustrate the effect. Both show a counts spectrum and single-temperature fit for a typical, unrelaxed cluster in our sample, with an aperture set at R_{2500} and a core region out to $0.15R_{2500}$ excised. Figure 1 is for a single-temperature model fit to the broad

band, while figure 2 is for the hard band. Note the excess emission relative to the model above 4.0 keV and the deficit below 2.5 keV that arises because the model cannot simultaneously fit both a hot component and a cooler, line-emitting component (Mazzotta et al. 2004). Figure 2 shows the same spectrum, but with the residuals for a model fit just to the hard band. In this case the fit is much better over the range from 2.0 to 7.0 keV but under-predicts the emission below 2.0 keV.

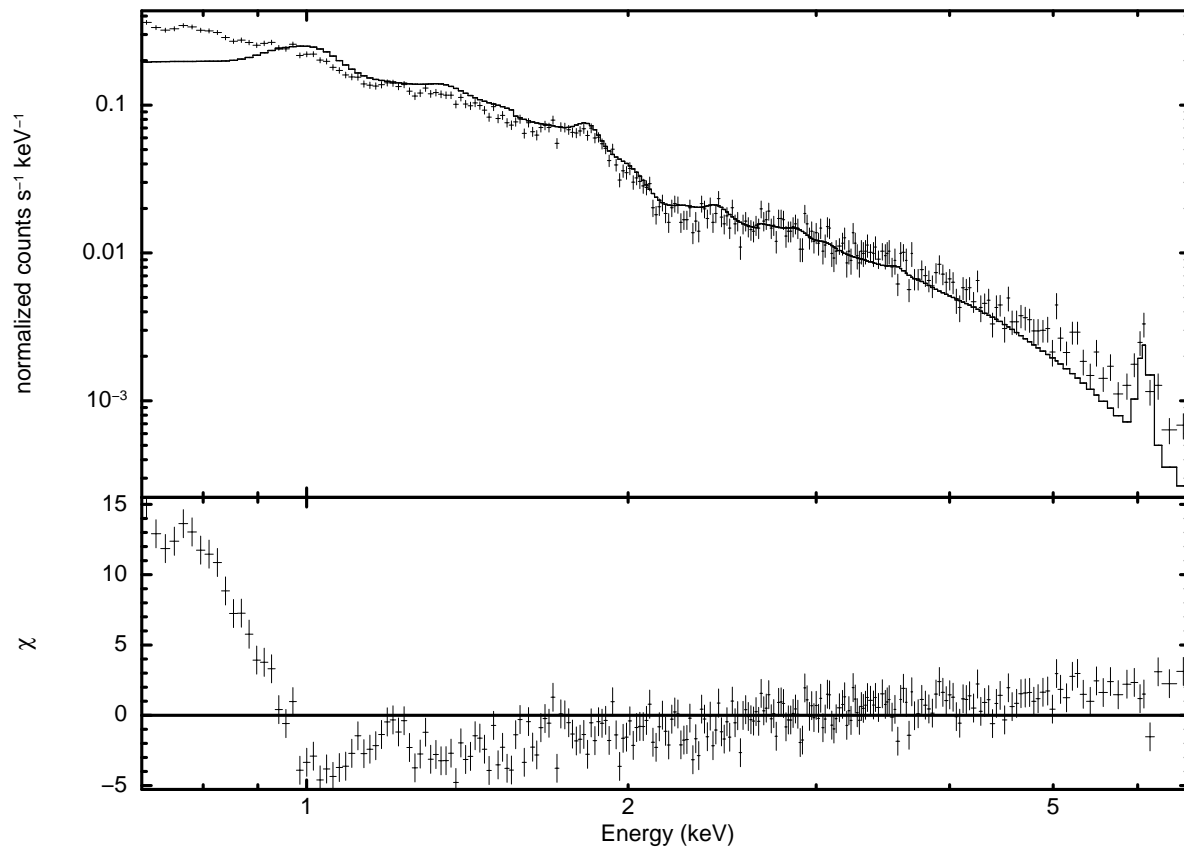
Mathiesen & Evrard (2001) suggested that the temperature skewing they observed might indicate a real temperature skewing detectable in real clusters using *Chandra*. Cavagnolo et al. (2008) fit single-temperature emission models to the hard band (2.0–7.0 keV) and broad band (0.7–7.0 keV) for a large ($N = 192$) sample of clusters with observations selected from the *Chandra* Data Archive. These authors show that for a large, heterogeneous sample of clusters across a broad temperature range, the distribution of T_{HBR} has a mean of 1.16 and an rms deviation $\sigma = \pm 0.10$, with T_{HBR} tending to be larger in merging systems. They also report that while this signal is significant in the aggregate, the errors for any single T_{HBR} measurement and the scatter across all of the measurements together pose challenges for any effort to use T_{HBR} either to select for merging systems or to obtain more accurate mass estimates. In order to meet these challenges it is important also to examine T_{HBR} and similar spectral signatures of dynamical state in a simulation context. Like the original study of Mathiesen & Evrard (2001), this paper examines the temperature ratio for a sample of simulated clusters and simulated *Chandra* observations, and as in the subsequent study by Valdarnini (2006), the simulated clusters analyzed here were generated using a hydrodynamical code with radiative cooling included.

This paper is organized as follows. In §2, we describe the simulated clusters in our sample along with the X-MAS code for generating their mock X-ray observations. In §3, we present our analysis methods and define the spectral signatures of dynamical state we examine. In §4, we report and discuss our results, and §5 summarizes our work.

2. Methods

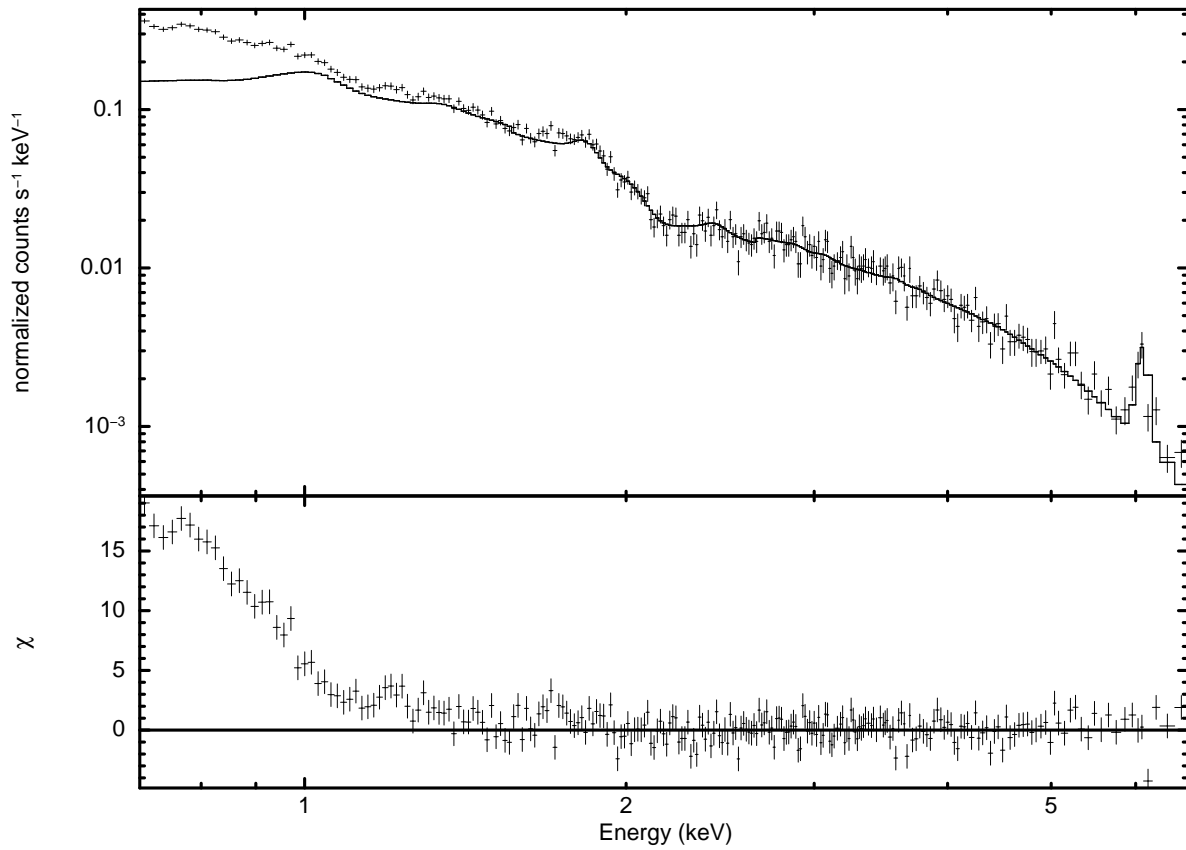
2.1. Numerical Simulations

This study is based on an analysis of 118 clusters simulated using the cosmological hydrodynamics TREE+SPH code GADGET-2 (Springel 2005), which were simulated in a standard Λ cold dark matter (Λ CDM) universe with matter density $\Omega_M = 0.3$, $h = 0.7$, $\Omega_b = 0.04$, and $\sigma_8 = 0.8$. The simulation includes radiative cooling assuming an optically-thin gas of primordial composition, with a time-dependent UV background from a population of



dventimi 14-Mar-2011 20:52

Fig. 1.— X-MAS simulated counts spectrum for a simulated cluster that appears to have significant temperature structure. A single-temperature MEKAL model fit to the [0.7–7.0] keV broad band is over-plotted as the solid line, with $k_B T = 2.42 \pm 0.03$ keV. Fit residuals appear in the bottom panel. This figure and Figure 2 illustrate qualitatively the effect that additional cool components have on a single-temperature fit.



dventimi 14-Mar-2011 20:50

Fig. 2.— X-MAS simulated counts spectrum for the same simulated cluster as in the previous figure. A single-temperature MEKAL model fit to the [2.0–7.0] keV hard band is over-plotted as the solid line, with $k_B T = 3.52 \pm 0.2$ keV. Fit residuals appear in the bottom panel.

quasars, and handles star formation and supernova feedback using a two-phase fluid model with cold star-forming clouds embedded in a hot medium. All but four of the clusters are from the simulation described in Borgani (2004), who simulated a box $192 h^{-1}$ Mpc on a side, with 480^3 dark matter particles and an equal number of gas particles. The present analysis considers the 114 most massive clusters within this box at $z = 0$, which all have M_{200} greater than $5 \times 10^{13} h^{-1} M_{\odot}$. These are referred to as the B04 Sample in the remainder of this paper. By convention, M_{Δ} refers to the mass contained in a sphere which has a mean density of Δ times the critical density ρ_c , and whose radius is denoted by R_{Δ} .

That cluster set covers the ~ 1.5 -5 keV temperature range, but the $192 h^{-1}$ Mpc box is too small to contain significantly hotter clusters. We therefore supplemented it with four clusters with masses $> 10^{15} h^{-1} M_{\odot}$ and temperatures > 5 keV drawn from a dark-matter-only simulation in a larger $479 h^{-1}$ Mpc box (Dolag & Stasyszyn 2009), referred to in this paper as the D09 sample. The cosmology for this simulation also was Λ CDM, but with $\sigma_8 = 0.9$. These were then re-simulated including hydrodynamics, radiative cooling, and star formation, again with GADGET-2 and using the zoomed-initial-conditions technique of Tormen (1997), with a fourfold increase in resolution. This is comparable to the resolution of the clusters in the smaller box. Adding these four massive clusters to our sample gives a total of 118 clusters with M_{200} in the range $5 \times 10^{13} h^{-1} M_{\odot}$ to $2 \times 10^{15} h^{-1} M_{\odot}$. The mean structural properties of massive clusters drawn from a sample with $\sigma_8 = 0.9$ may differ somewhat from those of similar-mass clusters in a $\sigma_8 = 0.8$ universe because they reflect a more advanced state of cosmic evolution. However, these four additional clusters carry minimal statistical weight in the context of the overall sample. They are included primarily to evaluate whether the mean and dispersion of their T_{HBR} values are consistent with those of the lower-mass systems.

2.2. X-Ray Simulations

The simulated galaxy clusters in our sample are processed with the *X-ray Map Simulator* version 2 (X-MAS) (Gardini et al. 2004; Rasia et al. 2008) to generate X-ray images suitable for standard *Chandra* reduction techniques. In its first step X-MAS uses the outputs of the hydrodynamic code to calculate the emissivity of each simulation element within the chosen field of view and to project this onto the image plane. In its second step it convolves the resulting flux with the appropriate response of a given detector. In the case of our simulated *Chandra* observations, the second step applies the response matrix file and ancillary response file for the ACIS S3 CCD, with a 200 kilosecond exposure time. In order to separate out potential calibration issues from the focus of this particular study, these response matrices

implement a constant response over the detector, and in generating the simulated X-ray images, the evolved zero-redshift clusters are shifted to a redshift sufficient to fit R_{500} within the 16 arcminute field of view. Because of this step, though the clusters in the sample are distributed over a range of physical sizes, they all have approximately the same apparent size projected onto the image plane and into the simulated observations.

2.3. M - T_X Relation

In this paper, cluster mass refers to M_{200} , while T_X refers to our estimated “spectral-fit temperatures” obtained using XSPEC (Arnaud 1996) to fit single-temperature MEKAL plasma models to various energy bands in simulated X-MAS X-ray observations taken from the numerically-simulated clusters. The steps involved in the process are described in detail in § 3.

Figure 3 shows the mass-temperature relation based on our sample of simulated clusters and estimated spectral fit temperatures, measured in a broad 0.7–7 keV band within an annular aperture from $0.15R_{500}$ to R_{2500} as in Cavagnolo et al. (2008). The best fits to the power-law form

$$M = M_0 \left(\frac{T_X}{2 \text{ keV}} \right)^\alpha \quad (1)$$

have the coefficients $M_0 = 1.09 \pm 0.01 \times 10^{14} h^{-1} M_\odot$, $\alpha = 1.57 \pm 0.06$ for the full sample of clusters. For the subset of clusters with $T_{2.0-7} > 2.0 \text{ keV}$, the best-fit parameters are $M_0 = 1.06 \pm 0.02 \times 10^{14} h^{-1} M_\odot$, $\alpha = 1.71 \pm 0.07$. As is generally the case for simulated clusters, the power-law indices of the mass-temperature relations found here are consistent with cluster self-similarity and the virial theorem (Kaiser 1986; Navarro et al. 1995). These relationships have scatter, which we characterize by the standard deviation in log space $\sigma_{\ln M}$ about the best-fit mass at fixed temperature T_X . We find $\sigma_{\ln M} = 0.10$.

3. Analysis

3.1. Filtering

We use X-MAS to simulate X-ray observations—provided as standard *Chandra* event files—then subject them to a series of reduction steps using the *Chandra* Interactive Analysis of Observations package (CIAO) v4.1 (Fruscione et al. 2006). All of the event files have at least 100K counts, while those for the most luminous clusters have over half a million counts. Simulated observations of this quality provide us with an opportunity to address the question

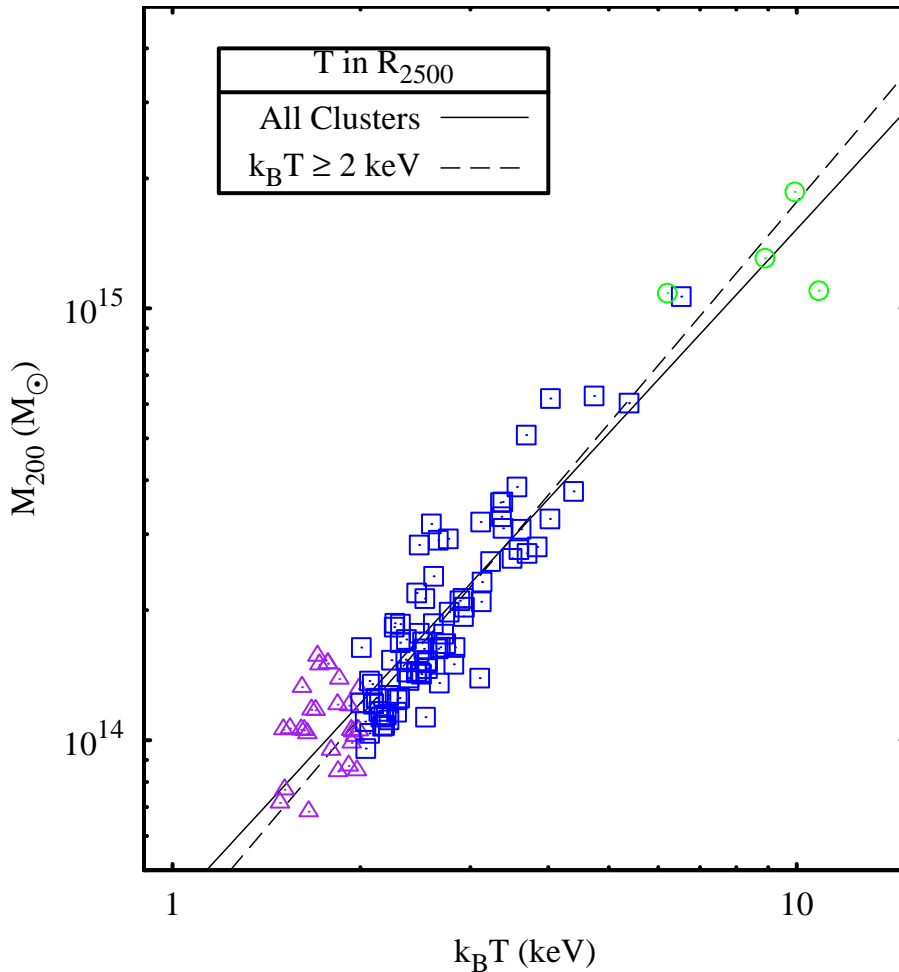


Fig. 3.— Mass-temperature (M - T_X) relation for the clusters in our sample. Clusters with $k_B T < 2$ keV are plotted in purple open triangles, while clusters with $k_B T \geq 2$ keV are plotted in blue open squares, and the four massive D09 clusters in green open circles. Mean relations are plotted with solid lines for the whole sample, and dashed lines for clusters with $k_B T \geq 2$ keV. Finally, note that average temperatures are taken within a core-excised annulus whose outer radius is placed at R_{2500} . [See the electronic edition of the Journal for a color version of this figure.]

of how much of the scatter in our temperature-structure statistics is intrinsic. Consequently, our first reduction step filters each raw event file into a new set of event files by randomly sampling the events it records. The number of counts in each file is its “count level,” and in order to cover the space of typical *Chandra* archival observations, we apply the filtering step to each of the raw event files four times, at count levels 15K, 30K, 60K, and 120K. These count levels roughly map to the range between observations of short duration or of relatively low surface-brightness objects to observations of long duration or of relatively high surface-brightness objects.

3.2. Cool Lump Excision

An example of a filtered event file appears in Figure 4 as a surface-brightness image. It displays a common feature of numerical simulations of galaxy clusters, which is the presence of relatively dense, cool, and metal-rich substructures that continuously undergo mass accretion and have not yet come into thermal equilibrium with the hot ICM surrounding them (Borgani & Kravtsov 2009). These bright point-like spots, or “cool lumps”, typically are associated with the dense cool cores of smaller halos that have merged with the primary halo. Generally regarded as an unphysical artifact of numerical simulations, at least insofar as their temperatures, densities, and concentrations are concerned, commonly they are excised before further analysis is conducted (Rasia et al. 2006; Piffaretti & Valdarnini 2008; Nagai et al. 2007).

In order to study the effect that excising cool lumps has on measures of temperature substructure, we produce from the originals several new event files whose cool lumps have been excised to an increasing degree. The CIAO `wavdetect` tool identifies peaks in the photon distribution by correlating an event file’s image with a sequence of “Mexican-Hat” wavelet functions of differing scale sizes, measured in pixels, then generates a source list with associated region files. We use its default sequence of wavelet scale sizes in this analysis (2 and 4 pixels), though we apply the tool four times to each filtered event file, each time incrementing the multiplicative factor by which the source regions are scaled. In CIAO `wavdetect`, the parameter governing this multiplicative factor is `ellsigma` and in our study ranges between 0 to 3. A value of 0 for `ellsigma` is equivalent to “no masking” while a value of 3 corresponds to what we call “full masking”. The effect is to produce versions of each cluster observation with a range of masking. Note that the wavelet scale size is a constant fraction of the cluster size because all the clusters have been redshifted so that R_{500} fits in the field of view.

We finish the extraction phase of our analysis with the following steps. First, for every

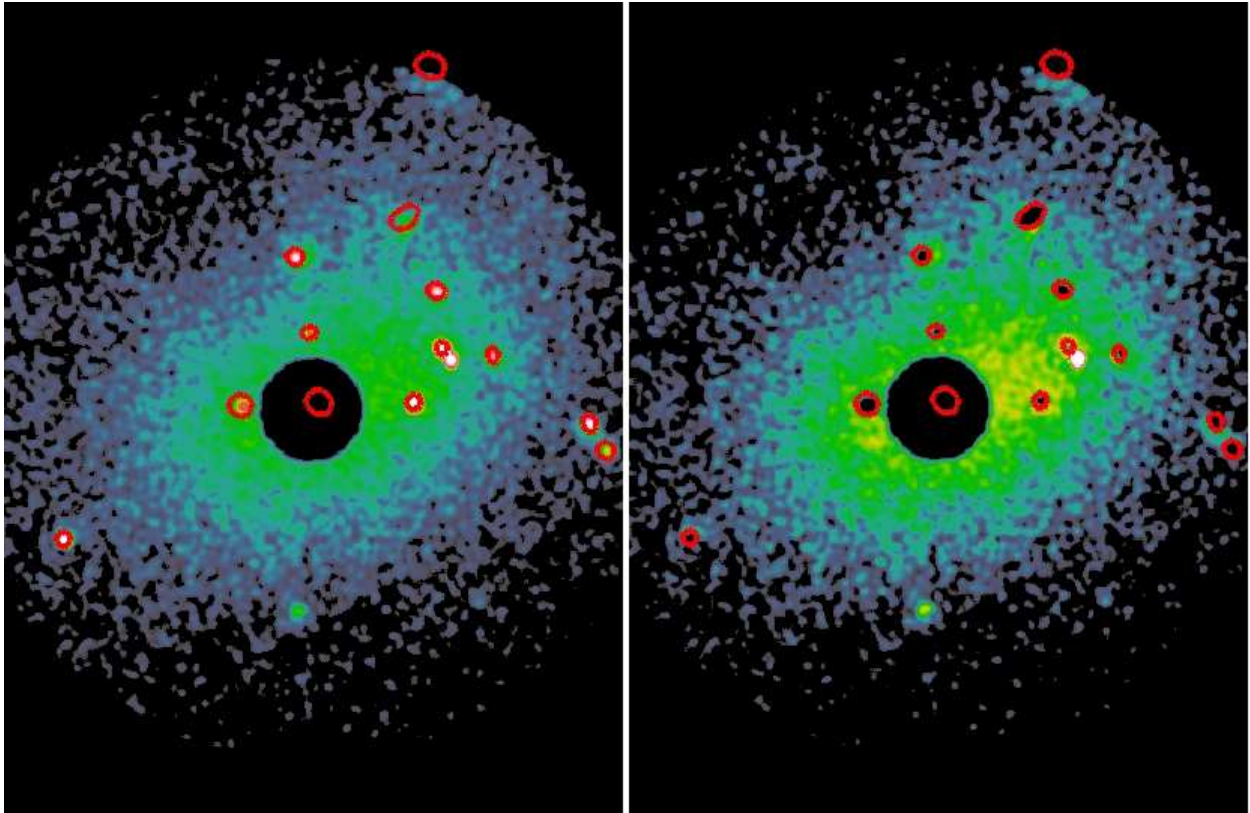


Fig. 4.— X-MAS simulated X-ray surface-brightness images for the same cluster whose spectrum is presented in Figures 1 and 2. The aperture is set at R_{2500} and a core region of size $0.15R_{2500}$ is excised. Note the surface-brightness peaks in the image. In this study these are detected automatically by the CIAO tool `wavdetect`, which generates source regions identified in this figure by red ellipses. Labeled “cool lumps” in this analysis, they are subjected to varying degrees of excision, from no masking (*left*) to full masking (*right*), as described in the text. [See the electronic edition of the *Journal* for a color version of this figure.]

excised file we apply an aperture of R_{2500} and excise the central $0.15 R_{2500}$ region, generating new copies of the event files. This step, including the centering algorithm, matches the procedure in Cavagnolo et al. (2008) so that regions measured in the simulated clusters correspond to those in the *Chandra* archival observations. Next, each fully-processed event file is extracted into a standard pulse-invariant (PI) spectral file binned so as to have at least 25 counts in each energy channel. The extraction phase is complete when each original raw event file generates PI spectral files suitable for spectral fitting in XSPEC.

3.3. Spectral Fitting

The PI spectral files are then fed into XSPEC v12.5.0 for spectral fitting. In order to form the temperature ratio T_{HBR} two fits are performed for each spectrum. The first fit is over the hard band from $2.0(1+z)^{-1}$ –7 keV, for which the $(1+z)^{-1}$ factor exists in order to shift the 2 keV cutoff from the observer’s frame to the cluster’s rest-frame. The simulated clusters occupy a range of redshifts because larger clusters are translated to higher redshifts in order to fit R_{500} within 16 arc-minutes, when creating artificial observations. The second fit is over the broad band, including all energy channels in the spectrum from 0.7–7 keV. Every fit is made by minimizing the χ^2 statistic for a single-temperature MEKAL model multiplied by a warm-absorber (WABS, to account for Galactic absorption). The Galactic column is fixed to $N_H = 5 \times 10^{20} \text{ cm}^{-2}$ and the metallicity to 0.3 Solar, leaving the temperature of the emission component, its H density (although this makes no difference), and its normalization as the only free parameters.

3.4. Quantifying Temperature Structure

We adopt two spectral measurements of temperature structure. The first is the temperature ratio T_{HBR} of Cavagnolo et al. (2008) and is found in the following way. For each simulated cluster in our sample, for each count level (15K, 30K, 60K, 120K), and for each cool lump masking level (0, 1, 2, 3), we find a spectral-fit temperature in the hard band and the broad band and form the temperature ratio T_{HBR} . Emission from cooler, line-emitting metal-rich parts of the ICM ought to be excluded from the hard band, so we expect that a T_{HBR} value greater than unity signals the presence of merging sub-clumps.

Our second measure of temperature, which we call the “cool residual,” (RES_{cool}) compares an observation’s actual broadband count rate to a model-predicted count rate for a spectral model fit only over the hard band. Again, we determined a spectral-fit temperature

for each combination of cluster, count level, and masking level, except that in this case we performed only a hardband fit. Since emission from cooler components should be excluded from this band, in general we achieve good fits even when the count level is sufficiently high that broadband fits may formally have large reduced χ^2 values. From this hardband model fit we estimate the corresponding broadband count rate and calculate its percentage deviation from the actual broadband count rate. While single-temperature systems will have actual count rates that are essentially the same as their model count rates, the introduction of cooler, luminous substructure components should generate an excess broadband count rate relative to the model. This measure of temperature substructure avoids the uncertainties associated with a single-temperature fit to the broad band.

4. Results and Discussion

Having calculated spectral-fit temperatures, T_{HBR} , and the cool residual for all of the clusters in our sample, we have the means to study how well temperature structure correlates with departures from the mean M - T_X relation, and how well these measures can be used to obtain better mass estimates. We will also examine how our results depend on the removal of the cool lumps.

4.1. T_{HBR} from Simulations.

We present in Figure 5 the temperature ratios T_{HBR} for our simulation sample, plotted as a function of the broadband temperature fit $T_{0.7-7}$. This figure is similar to Figure 8 in Cavagnolo et al. (2008), which shows that the mean value of T_{HBR} observed among clusters in the *Chandra* archive is $\langle T_{\text{HBR}} \rangle = 1.16$, with a standard deviation of $\sigma_{\text{THBR}} = 0.10$. We remind the reader of important differences between the two samples being considered. The *Chandra* archive sample of Cavagnolo et al. (2008) contains clusters most of which have $k_B T > 3$ keV, whereas most of the clusters in our sample have $k_B T < 3$ keV. Nevertheless, even with that caveat the temperature ratios of the simulated clusters are distributed in approximately the same way as are those in the real sample of Cavagnolo et al. (2008), with $\langle T_{\text{HBR}} \rangle = 1.12$ and $\sigma_{\text{THBR}} = 0.11$, provided the cool lumps are not excised (circles in Figure 5). When the cool lumps are excised (squares in Figure 5), the mean and variance of T_{HBR} diminish, with $\langle T_{\text{HBR}} \rangle = 1.07$ and $\sigma_{\text{THBR}} = 0.07$. These values are for the full 120K count data, though the full set of $\langle T_{\text{HBR}} \rangle$ for the four `ellsigma` values and four count values are tabulated in Table 1. This table provides mean values for T_{HBR} and its variance for all of the clusters in the sample, and for a subset whose $T_{2.0-7}$ value is greater than 2 keV. Much

of the variance derives from the lower-temperature clusters, and as they are removed the variance in T_{HBR} drops significantly, especially when full masking is applied.

Figure 6 presents a similar effect for RES_{cool} . Here, we see that the excision of cool lumps again reduces the mean and variance of the temperature substructure measure, although in this case the effect is more dramatic. Evidently, the presumably unphysical cool lumps in simulated clusters may be necessary to reproduce the distribution of quantitative temperature substructure measures found in real clusters. This is a subject which we return to in Section 4.3.

4.2. Temperature Structure and Scaling Relations

Our original motivation for conducting this study was to determine if temperature structure, as quantified by the temperature ratio T_{HBR} , correlates with and can be used to correct for departures from the mean mass-temperature relation $M-T_X$. In order to test this idea, we define the “mass offset” at fixed temperature by the relation

$$\delta \ln M(T_X) = \ln \left[\frac{M}{M_{\text{pred}}(T_X)} \right] \quad (2)$$

where M is the cluster’s actual mass, and M_{pred} is the mass predicted from the mean $M-T_X$ relation. Figure 7 plots the mass offsets for our simulated clusters as a function of T_{HBR} , for the case in which predicted masses are derived from the $M-T_X$ relation for the broadband spectral fit temperature. Values of T_{HBR} calculated both with cool lumps excised (squares) and without excision (circles) appear in this figure. Error bars on T_{HBR} are omitted for clarity. While there is some correlation, such that clusters with more temperature structure (larger T_{HBR}) tend to be more massive than predicted by the mean $M-T_X$ relation, the trend is weak and has substantial scatter. Excising the cool lumps weakens the trend further. Figure 8 shows the same comparison for the RES_{cool} measure instead of T_{HBR} , and in this case we again find that excising the cool lumps has an even larger effect for T_{HBR} although in both cases accounting for temperature substructure does not greatly reduce scatter in mass offset.

4.3. Effects of Masking Strategy

We now examine the decline in T_{HBR} and its variance as cool lumps are excised, beginning with Figure 9, which focuses on T_{HBR} . Here, we plot the statistic’s standard deviation σ_{THBR} as a function of the two dimensions along which we adjust our analysis pipeline, with

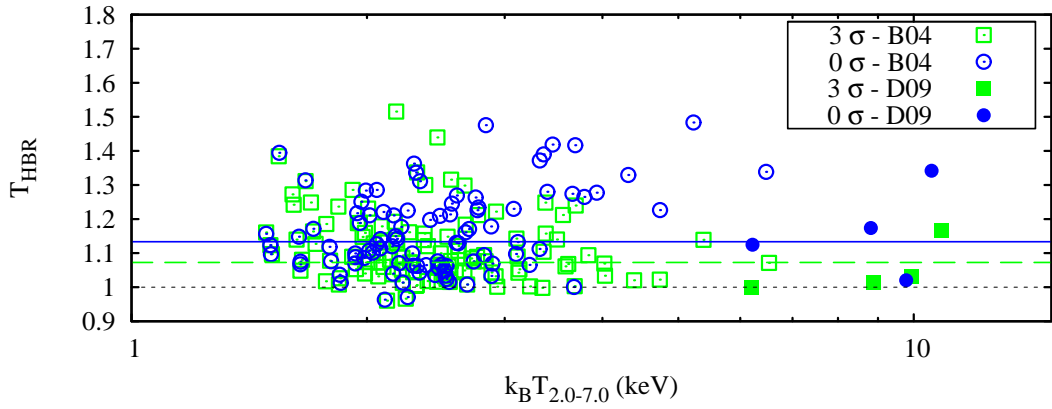


Fig. 5.— T_{HBR} plotted against $T_{0.7-7}$ for simulated X-MAS observations that have approximately 120K counts. Hydrodynamic simulations may produce spurious over-condensations of cool gas. These cool lumps can be excised using the CIAO tool `wavdetect`, whose aggressiveness can be controlled via its `ellsigma` parameter. Squares correspond to single-temperature MEKAL fits whose underlying observations are processed by `wavdetect` with `ellsigma` set to 3, and circles correspond to those with `ellsigma` set to 0. Finally, note that the 4 massive D09 clusters are denoted by filled symbols rather than by open symbols. The solid line represents the mean when cool lumps are not removed, while the dashed line represents the mean when they are removed. The dotted line indicates $T_{\text{HBR}} = 1$. [See the electronic edition of the *Journal* for a color version of this figure.]

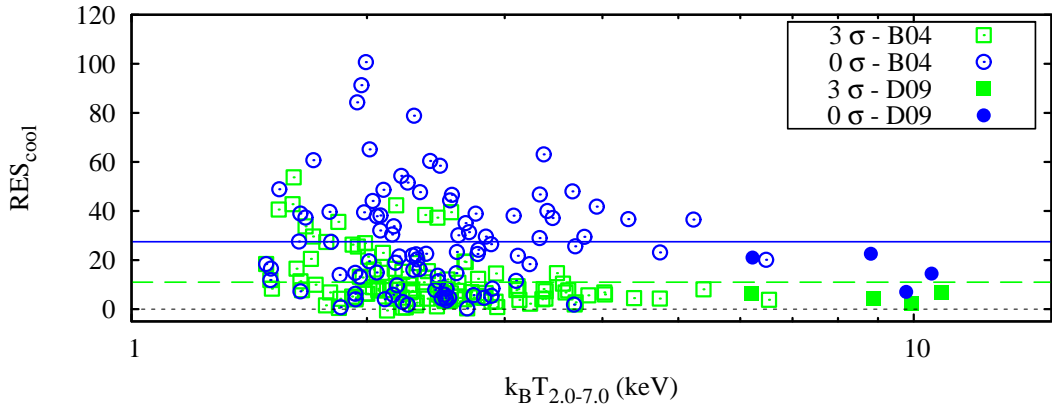


Fig. 6.— RES_{cool} plotted against $T_{0.7-7}$ for simulated X-MAS observations that have approximately 120K counts. This statistic tracks the percent excess count rate of the actual observation with respect to count rate for a MEKAL model fit to just the hard band. Squares correspond to single-temperature MEKAL fits whose underlying observations are processed by wvdetect with ellsigma set to 3, and circles correspond to those with ellsigma set to 0. As in the previous plot, the 4 massive D09 clusters are denoted by filled symbols rather than by open symbols. The solid line represents the mean when cool lumps are not removed, the dashed line represents the mean when they are removed, and the dotted line indicates zero residual. [See the electronic edition of the Journal for a color version of this figure.]

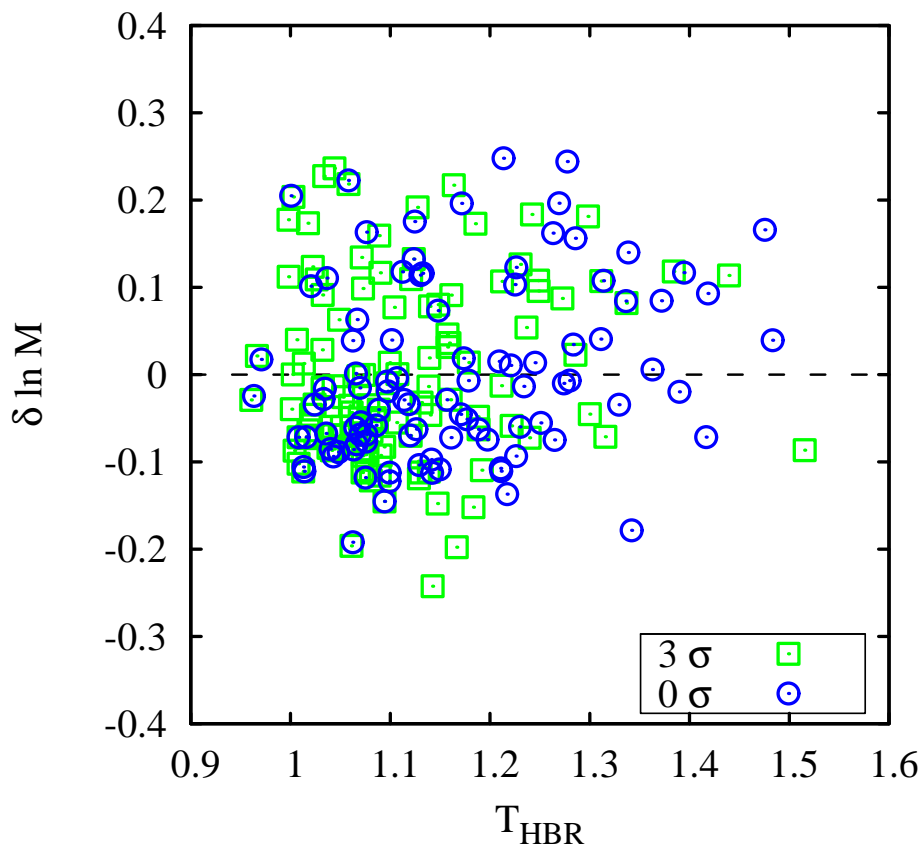


Fig. 7.— Relationship between T_{HBR} and mass offset $\delta \ln M(T_X)$ from the mean M - T_X relationship for the clusters in combined B04+D09 simulation sample. The temperatures in this relation are our broadband spectral-fit temperatures. Squares correspond to simulated X-MAS observations that are processed by wavdetect with ellsigma set to 3 (full masking), while circles correspond to observations that have ellsigma set to 0. [See the electronic edition of the Journal for a color version of this figure.]

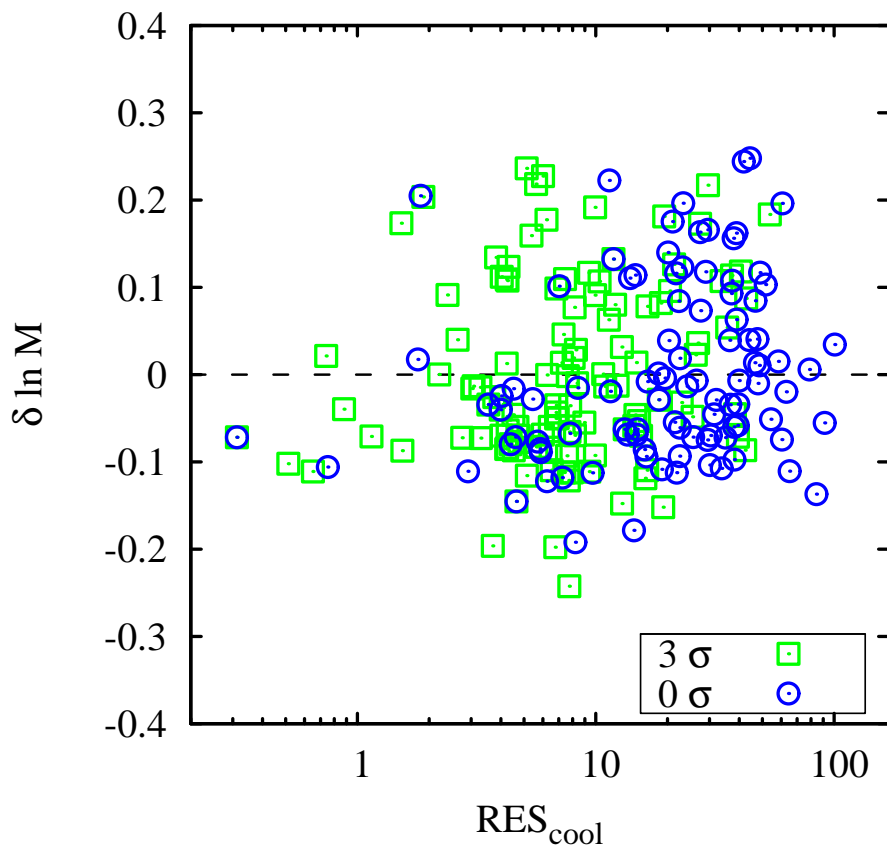


Fig. 8.— Relationship between RES_{cool} and mass offset $\delta \ln M(T_X)$ from the mean $M-T_X$ relationship for the clusters in combined B04+D09 simulation sample. The temperatures in this relation are our broadband spectral-fit temperatures. Squares correspond to simulated X-MAS observations that are processed by wavdetect with ellsigma set to 3, while circles correspond to observations that have ellsigma set to 0. [See the electronic edition of the *Journal* for a color version of this figure.]

the top panel devoted to the masking strategy, and the bottom panel devoted to the count level. Focusing on the top panel, we see that increasing the `ellsigma` parameter of the CIAO `wavdetect` tool from 0 to 3 reduces σ_{THBR} from 0.15 down to 0.13, when the observations are relatively “poor” (with $\sim 15\text{K}$ counts). With higher-quality observations of 60K or 120K counts, the decline in σ_{THBR} is greater, going from 0.12 down to 0.07 as the `ellsigma` parameter rises from 0 to 3, and σ_{THBR} for full masking ends up being significantly less than the value of 0.10 observed in the Cavagnolo et al. (2008) sample.

Figure 10 helps show why the temperature ratio T_{HBR} and its variance decline as the cool lumps are removed. It plots the sample average of the relative change in temperature as the CIAO `wavdetect` `ellsigma` parameter is increased. As more of each cool lump is excised, both the broadband spectral fit temperature, and the hardband fit temperature increase. However, the increase is significantly larger for the broadband temperature, as the cool lumps’ contribution to the flux is already largely excluded from the hardband fits. The top panel in this figure shows this effect for spectra with approximately 120K counts, while the bottom panel is for spectra with approximately 15K counts.

Another way of visualizing the effect of more aggressive masking is depicted in Figure 11. The top panel in this figure is similar to Figure 6 in that it occupies the $T_{0.7-7}-T_{\text{HBR}}$ plane, with T_{HBR} plotted as a function of $T_{0.7-7}$ for our simulated clusters. Arrows illustrate the shift in T_{HBR} and in $T_{0.7-7}$, as the cool lumps are excised. Some of the clusters experience very large shifts in both quantities, while others experience no shifts at all. The former are associated with clusters that have many well-defined and bright cool lumps, while the latter correspond to those clusters that are completely free of cool lumps. The bottom panel in this figure shows just the size of this shift for the T_{HBR} statistic, from which we can see that some clusters indeed have a shift of precisely 0. Again, these are clusters whose simulated X-ray observations are unchanged after applying the CIAO `wavdetect` tool because it finds no sources to mask out.

4.4. Substructure Measures and T_{HBR}

Various researchers have established a clear correlation between morphological measures of cluster dynamical state and $\delta \ln M$ (Jeltema et al. 2008; Ventimiglia et al. 2008; Piffaretti & Valdarnini 2008; Yang et al. 2009), a correlation which is less apparent in our study of spectral measures of substructure. Similarly, Cavagnolo et al. (2008) found a correlation between the temperature ratio and structure for their *Chandra* sample, in that merging events are associated with elevated T_{HBR} . To probe this issue further we focus on T_{HBR} and compare it to several metrics for cluster substructure. These are the centroid

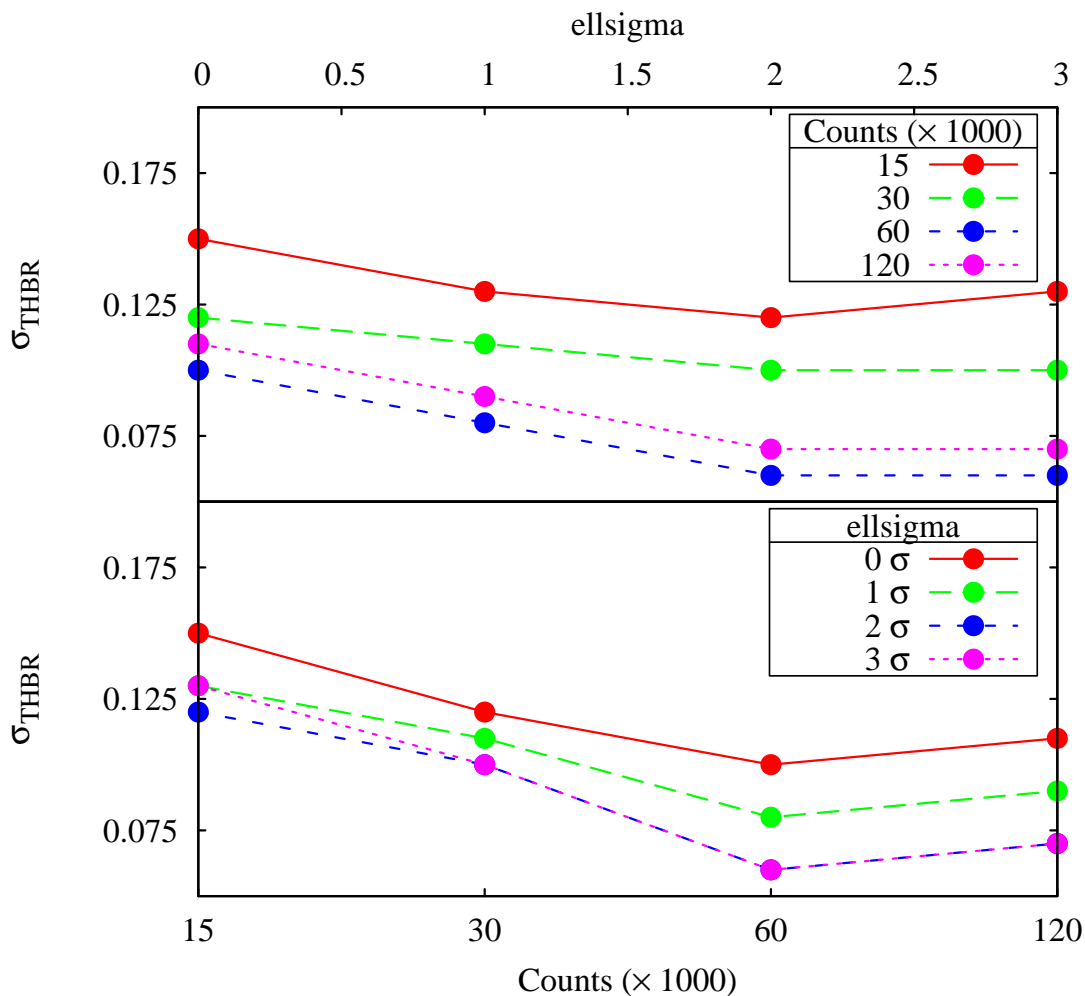


Fig. 9.— (*top*) Decline in the T_{HBR} standard deviation $\sigma_{T_{\text{HBR}}}$ as *wavdetect*'s ellsigma parameter ranges from 0 to 3. These are plotted for a family of simulated observations of increasingly higher quality, from approximately 15k counts to approximately 120k counts. (*bottom*) Decline in $\sigma_{T_{\text{HBR}}}$ as simulated X-MAS observations go from lowest-quality (approximately 15k counts) to highest-quality (approximately 120k counts). These are plotted for a family of simulated observations with *wavdetect*'s ellsigma parameter ranges from 0 to 3. [See the electronic edition of the Journal for a color version of this figure.]

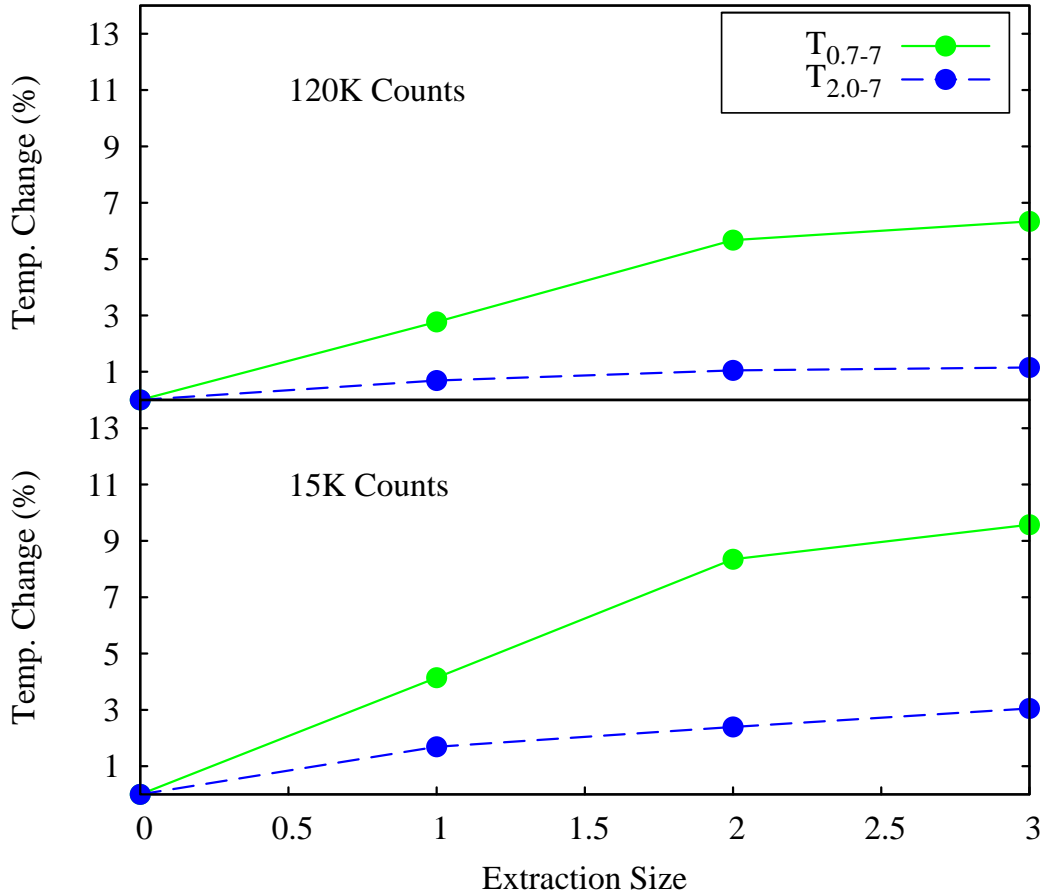


Fig. 10.— Relative change in spectral fit temperatures as the cool lumps are removed from the simulated clusters for high-quality simulated observations. (*top*) Observations with approximately 120K counts. (*bottom*) Observations with approximately 15K counts. Note that these are for observations in an aperture corresponding to R_{2500} . [See the electronic edition of the Journal for a color version of this figure.]

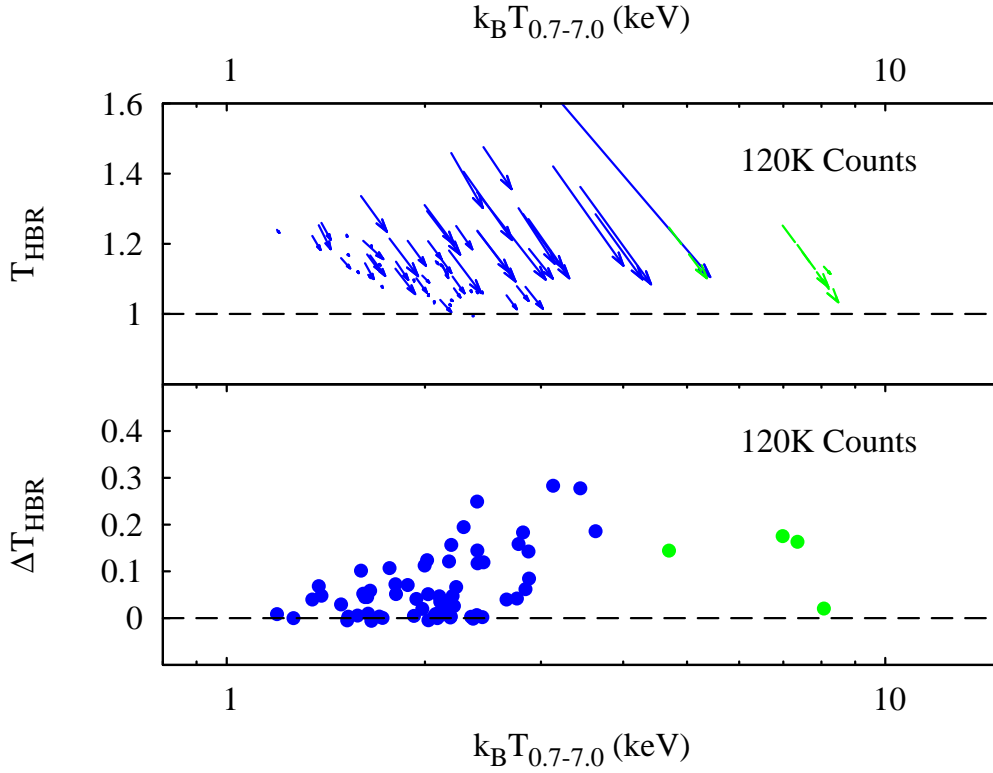


Fig. 11.— (*Top*) Shift in the $T_{0.7-7}-T_{\text{HBR}}$ plane as wavdetect’s ellsigma parameter ranges from 0 to 3. Clusters from the B04 sample are depicted with solid arrows, while clusters from the D09 sample are depicted with long-dashed arrows. broadband spectral-fit temperatures are estimated within an aperture set at R_{2500} . Notice that the distribution of most of the points shifts significantly to higher spectral fit temperatures and smaller temperature ratios as cool lumps are excised. Notice also that some simulated clusters are unaffected by cool lumps, so that their net shift is 0. (*Bottom*) The T_{HBR} component (y-axis) of the shift presented in the top panel. Note that these are for simulated X-MAS observations of maximum quality, having approximately 120K counts. [See the electronic edition of the Journal for a color version of this figure.]

variation w , the axial ratio η , and the power ratios P_{20} and P_{30} (see Ventimiglia et al. 2008, and references therein). The centroid variation w measures the skewness of a cluster’s two-dimensional photon distribution by calculating the variance in a series of isophotes for the cluster surface-brightness map. The axial ratio η measures a cluster’s elongation, which tends to increase during merger events. The power ratios P_{20} and P_{30} decompose a cluster’s surface-brightness image into two-dimensional multipole expansions, capturing different aspects of a cluster’s geometry. P_{20} relates to the ellipticity in an image and is similar to the axial ratio η , while P_{30} measures the “triangularity” in an image.

In Ventimiglia et al. (2008) we calculated these morphological substructure metrics for a superset of the B04 sample of simulated galaxy clusters and compared them to departures from the M - T_X relation (see Fig. 8 in that paper). Here we use the same substructure measures for the 114 B04 clusters for which we are able to calculate T_{HBR} and compare the results. These are presented in Figure 12. Whereas in Ventimiglia et al. (2008) there is a clear correlation between morphological substructure and $\delta \ln M$, we find in this study that there is little or no correlation between substructure and T_{HBR} for our B04 sample.

In order to understand how temperature structure and morphological structure can be uncorrelated, we looked at four simulated clusters having approximately the same temperature ($k_B T \simeq 3.2 \text{keV}$) and occupying the relative extremes in T_{HBR} and in the centroid variation w . Two were selected for relatively low T_{HBR} ($\simeq 1.1$) but large variation in w ($\simeq 0.02$ – 1.0). Two were selected for large T_{HBR} ($\simeq 1.4$) but again large variation in the morphological structure parameter ω ($\simeq 0.1$ – 1.0). These clusters are presented in Figure 13 with surface-brightness contours overplotted and with the associated values for T_{HBR} and w . The two clusters in the left column appear more symmetric in their contours, while the two in the right column exhibit noticeable centroid shift. However, the morphologically apparent structure in the lower right cluster is not observed spectrally in the temperature ratio T_{HBR} . Evidently, neither morphology nor T_{HBR} is a perfect measure of relaxation in our simulation sample, as it contains clusters with small centroid shift ω and obvious substructure, as in the upper left of this figure. And, it contains clusters with large w that are nearly isothermal, as in the lower right of this figure.

5. Summary

We used a sample of galaxy clusters simulated with radiative cooling and supernova feedback, along with simulated *Chandra* X-ray observations of these clusters, to study temperature inhomogeneity as a signature of cluster dynamical state. Specifically, we adopted two methods of quantifying temperature inhomogeneity spectroscopically, the temperature

ratio T_{HBR} (Mathiesen & Evrard 2001; Cavagnolo et al. 2008) and the cool residual RES_{cool} . The former is the ratio of a hardband X-ray spectral-fit temperature to a broadband temperature, and becomes greater than 1 for clusters whose ICM contains cool, over-luminous sub-components. The latter is the excess broadband count rate relative to the count rate predicted by a model fit to the hard X-ray band. Though our simulated clusters are typically less massive and have lower temperatures than the *Chandra* archive clusters in Cavagnolo et al. (2008), we find that their temperature ratios T_{HBR} occupy generally the same distribution as the observed clusters.

We also looked for an opportunity to combine T_{HBR} and the cool residual with the mean mass-temperature relation to obtain better mass estimates than are achieved just with the scaling relation alone. We find, however, that while both T_{HBR} and the RES_{cool} are correlated with offset from the M - T_X relation, these correlations are weak, at least for this sample. We conclude that these measures of temperature inhomogeneity are not very effective at reducing scatter in the mass-temperature relation.

Finally, we note a particular difficulty that arises when trying to use clusters from hydrodynamic simulations to calibrate scatter-correction observables based on temperature inhomogeneity, such as T_{HBR} . Historically, simulated clusters have tended to exhibit their own kind of “over-cooling problem”, in which dense lumps of luminous, cool gas associated with merged sub-halos appear. These cool lumps are often excised from simulated clusters before their global properties are measured, but masking them appears to make the remaining temperature structure of the simulated clusters overly homogeneous. This finding suggests that real clusters may have cooler sub-components, that are more diffuse and less concentrated than in their simulated counterparts. Some physical process, perhaps thermal conduction, turbulent heat transport (e.g., Dennis & Chandran 2005; Parrish, Quataert & Sharma 2010; Ruszkowski & Oh 2011), or a more aggressive form of feedback, prevents cool lumps from forming in real clusters and might not completely eliminate those temperature inhomogeneities. Newer simulations incorporate treatments of conduction and AGN feedback, as well as more accurate treatments of mixing, and it will be interesting to revisit these temperature inhomogeneity measures in simulated clusters when large samples of such simulated clusters become available.

The authors wish to thank Stefano Borgani for contributing the simulation data on which this project was based. This work was supported by NASA through grants NNG04GI89G and NNG05GD82G, through Chandra theory grant TM8-9010X, and through Chandra archive grant SAOAR5-6016X. Some of it was done at the Kavli Institute for Theoretical Physics in Santa Barbara, supported in part by the National Science Foundation under Grant No. NSF PHY05-51164.

REFERENCES

- Arnaud, K. A. 1996, in *Astronomical Society of the Pacific Conference Series*, Vol. 101, *Astronomical Data Analysis Software and Systems V*, ed. G. H. Jacoby & J. Barnes, 17–+
- Borgani, S. 2004, *Astrophysics and Space Science*, 294, 51
- Borgani, S., & Kravtsov, A. 2009, *ArXiv e-prints*
- Buote, D. A., & Tsai, J. C. 1995, *Astrophysical Journal*, 452, 522
- Cavagnolo, K. W., Donahue, M., Voit, G. M., & Sun, M. 2008, *Astrophysical Journal*, 682, 821
- Cunha, C. E., & Evrard, A. E. 2010, *Phys. Rev. D*, 81, 083509
- Dennis, T. J., & Chandran, B. D. G. 2005, *ApJ*, 622, 205
- Dolag, K., & Stasyszyn, F. 2009, *MNRAS*, 398, 1678
- Eisenstein, D. J., Zehavi, I., Hogg, D. W., Scoccamarro, R., Blanton, M. R., Nichol, R. C., Scranton, R., Seo, H., Tegmark, M., Zheng, Z., Anderson, S. F., Annis, J., Bahcall, N., Brinkmann, J., Burles, S., Castander, F. J., Connolly, A., Csabai, I., Doi, M., Fukugita, M., Frieman, J. A., Glazebrook, K., Gunn, J. E., Hendry, J. S., Hennessy, G., Ivezi, Z., Kent, S., Knapp, G. R., Lin, H., Loh, Y., Lupton, R. H., Margon, B., McKay, T. A., Meiksin, A., Munn, J. A., Pope, A., Richmond, M. W., Schlegel, D., Schneider, D. P., Shimasaku, K., Stoughton, C., Strauss, M. A., SubbaRao, M., Szalay, A. S., Szapudi, I., Tucker, D. L., Yanny, B., & York, D. G. 2005, *Astrophysical Journal*, 633, 560
- Fabjan, D., Borgani, S., Rasia, E., Bonafede, A., Dolag, K., Murante, G., & Tornatore, L. 2011, *arXiv:1102.2903*
- Frieman, J. A., Turner, M. S., & Huterer, D. 2008, *Annual Review of Astronomy and Astrophysics*, 46, 385
- Fruscione, A., McDowell, J. C., Allen, G. E., Brickhouse, N. S., Burke, D. J., Davis, J. E., Durham, N., Elvis, M., Galle, E. C., Harris, D. E., Huenemoerder, D. P., Houck, J. C., Ishibashi, B., Karovska, M., Nicastro, F., Noble, M. S., Nowak, M. A., Primini, F. A., Siemiginowska, A., Smith, R. K., & Wise, M. 2006, in *CIAO: Chandra’s data analysis system*, Vol. 6270, 60

- Gardini, A., Rasia, E., Mazzotta, P., Tormen, G., Grandi, S. D., & Moscardini, L. 2004, *Monthly Notices of the Royal Astronomical Society*, 351, 505
- Jeltema, T. E., Hallman, E. J., Burns, J. O., & Motl, P. M. 2008, *Astrophysical Journal*, 681, 167
- Kaiser, N. 1986, *Monthly Notices of the Royal Astronomical Society*, 222, 323
- Kravtsov, A. V., Vikhlinin, A., & Nagai, D. 2006, *Astrophysical Journal*, 650, 128
- Lima, M., & Hu, W. 2005, *Physical Review D*, 72, 43006
- Mantz, A., Allen, S. W., Rapetti, D., & Ebeling, H. 2010, *MNRAS*, 406, 1759
- Mathiesen, B. F., & Evrard, A. E. 2001, *Astrophysical Journal*, 546, 100
- Mazzotta, P., Rasia, E., Moscardini, L., & Tormen, G. 2004, *MNRAS*, 354, 10
- Mohr, J. J., & Evrard, A. E. 1997, *Astrophysical Journal*, 491, 38
- Mohr, J. J., Fabricant, D. G., & Geller, M. J. 1993, *Astrophysical Journal*, 413, 492
- Nagai, D., Kravtsov, A. V., & Vikhlinin, A. 2007, *Astrophysical Journal*, 668, 1
- Navarro, J. F., Frenk, C. S., & White, S. D. M. 1995, *Monthly Notices of the Royal Astronomical Society*, 275, 720
- Norman, M. L., & Bryan, G. L. 1999, in *Cosmological Adaptive Mesh Refinement* CD, Vol. 240, 19
- O’Hara, T. B., Mohr, J. J., Bialek, J. J., & Evrard, A. E. 2006, *Astrophysical Journal*, 639, 64
- O’Shea, B. W., Bryan, G., Bordner, J., Norman, M. L., Abel, T., Harkness, R., & Kritsuk, A. 2004, *Introducing Enzo, an AMR Cosmology Application*, <http://adsabs.harvard.edu/abs/2004astro.ph..3044O>
- Parrish, I. J., Quataert, E., & Sharma, P. 2010, *ApJ*, 712, 194
- Perlmutter, S., Aldering, G., Goldhaber, G., Knop, R. A., Nugent, P., Castro, P. G., Deustua, S., Fabbro, S., Goobar, A., Groom, D. E., Hook, I. M., Kim, A. G., Kim, M. Y., Lee, J. C., Nunes, N. J., Pain, R., Pennypacker, C. R., Quimby, R., Lidman, C., Ellis, R. S., Irwin, M., McMahon, R. G., Ruiz-Lapuente, P., Walton, N., Schaefer, B., Boyle, B. J., Filippenko, A. V., Matheson, T., Fruchter, A. S., Panagia, N., Newberg, H. J. M., Couch, W. J., & Project, T. S. C. 1999, *Astrophysical Journal*, 517, 565

- Piffaretti, R. & Valdarnini, R. 2008, *A&A*, 491, 71
- Rasia, E., Etti, S., Moscardini, L., Mazzotta, P., Borgani, S., Dolag, K., Tormen, G., Cheng, L. M., & Diaferio, A. 2006, *MNRAS*, 369, 2013
- Rasia, E., Mazzotta, P., Bourdin, H., Borgani, S., Tornatore, L., Etti, S., Dolag, K., & Moscardini, L. 2008, *Astrophysical Journal*, 674, 728
- Rasia, E., Meneghetti, M., Martino, R., Borgani, S., Bonafede, A., Dolag, K., Etti, S., Fabjan, D., Giocoli C., Mazzotta, P., Merten, J., Radovich, M., & Tornatore, L. 2011, *New Journal of Physics*, in press
- Riess, A. G., Filippenko, A. V., Challis, P., Clocchiatti, A., Diercks, A., Garnavich, P. M., Gilliland, R. L., Hogan, C. J., Jha, S., Kirshner, R. P., Leibundgut, B., Phillips, M. M., Reiss, D., Schmidt, B. P., Schommer, R. A., Smith, R. C., Spyromilio, J., Stubbs, C., Suntzeff, N. B., & Tonry, J. 1998, *Astronomical Journal*, 116, 1009
- Ruszkowski, M., & Oh, S. P. 2011, *ApJ*, 414, 1493
- Springel, V. 2005, *Monthly Notices of the Royal Astronomical Society*, 364, 1105
- Stanek, R., Rasia, E., Evrard, A. E., Pearce, F., & Gazzola, L. 2011, *ApJ*, 715, 1508
- Tormen, G. 1997, *Monthly Notices of the Royal Astronomical Society*, 290, 411
- Valdarnini, R. 2006, *New Astronomy*, 12, 71
- Ventimiglia, D. A., Voit, G. M., Donahue, M., & Ameglio, S. 2008, *Astrophysical Journal*, 685, 118
- Vikhlinin, A., Kravtsov, A. V., Burenin, R. A., Ebeling, H., Forman, W. R., Hornstrup, A., Jones, C., Murray, S. S., Nagai, D., Quintana, H., & Voevodkin, A. 2009, *Astrophysical Journal*, 692, 1060
- Yang, H. K., Ricker, P. M., & Sutter, P. M. 2009, *Astrophysical Journal*, 699, 315

Table 1. T_{HBR} & $\sigma_{T_{\text{HBR}}}$

counts	ellsigma	$\overline{T_{\text{HBR}}^{\text{a}}}$	$\overline{\sigma}^{\text{a}}$	$\overline{T_{\text{HBR}}^{\text{b}}}$	$\overline{\sigma}^{\text{b}}$
15000	0	1.19	0.15	1.20	0.15
15000	1	1.17	0.13	1.18	0.13
15000	2	1.13	0.12	1.13	0.11
15000	3	1.13	0.13	1.13	0.12
30000	0	1.16	0.12	1.16	0.12
30000	1	1.13	0.11	1.13	0.11
30000	2	1.10	0.10	1.10	0.10
30000	3	1.10	0.10	1.09	0.10
60000	0	1.13	0.10	1.14	0.10
60000	1	1.11	0.08	1.11	0.08
60000	2	1.08	0.06	1.08	0.06
60000	3	1.07	0.06	1.07	0.06
120000	0	1.12	0.11	1.12	0.12
120000	1	1.10	0.09	1.10	0.09
120000	2	1.07	0.07	1.07	0.07
120000	3	1.07	0.07	1.07	0.06

^aAll Clusters

^bClusters with $k_B T_{2.0-7} > 2$ keV

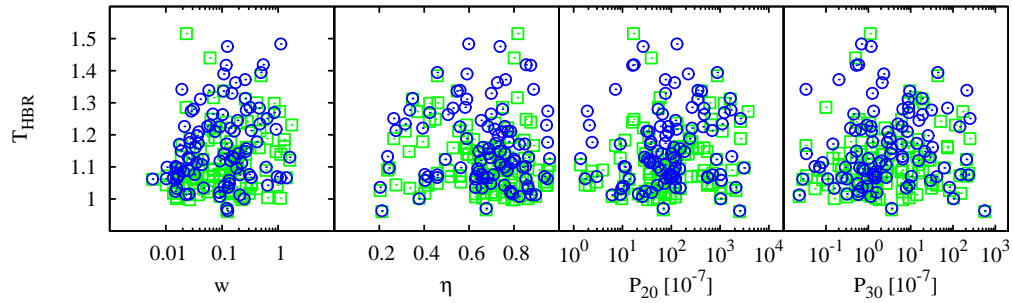


Fig. 12.— Relationship between T_{HBR} and four measures of substructure: the axial ratio η , the centroid variation w , and the power ratios P_{20} and P_{30} . Squares correspond to simulated X-MAS observations that are processed by wavdetect with ellsigma set to 3 (full masking), while circles correspond to observations that have ellsigma set to 0. [See the electronic edition of the Journal for a color version of this figure.]

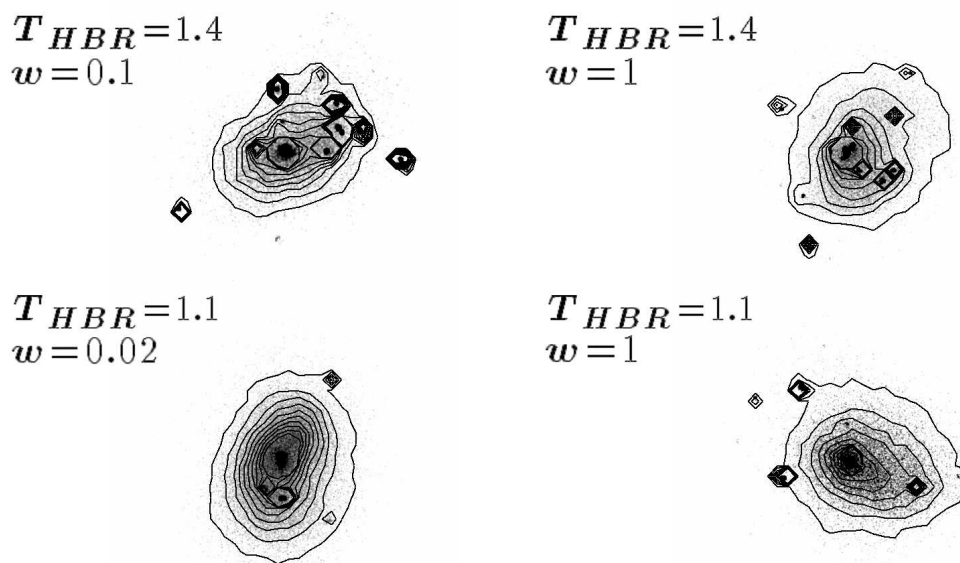


Fig. 13.— Surface-brightness contours for four clusters drawn from our simulation sample, illustrating that temperature ratio and centroid shift are both imperfect measures of relaxation. All four clusters are at nearly the same temperature, with $k_B T \simeq 3.2$. The two in the left column exhibit little centroid shift w , while the two in the right column have centroid shift near the maximum for the sample. The two clusters in the bottom row have low T_{HBR} while the two in the top row have higher T_{HBR} suggesting the presence of multiple temperature components.